RESEARCH ARTICLE | NOVEMBER 16 2023

Pushing the heterometal doping limit while preserving longlived charge separation in a Ti-based MOF photocatalyst *⊙*

Conor L. Long ⑩ ; Xiaoyi Zhang ⑩ ; Jenny V. Lockard **▼** ⑩



J. Chem. Phys. 159, 194704 (2023) https://doi.org/10.1063/5.0174664





CrossMark





Pushing the heterometal doping limit while preserving long-lived charge separation in a Ti-based MOF photocatalyst

Cite as: J. Chem. Phys. 159, 194704 (2023); doi: 10.1063/5.0174664 Submitted: 1 September 2023 · Accepted: 19 October 2023 · **Published Online: 16 November 2023**











Conor L. Long, Diagoni Zhang, Diagoni Jenny V. Lockard Diagoni



AFFILIATIONS

- Department of Chemistry, Rutgers University-Newark, Newark, New Jersey 07102, USA
- ²X-ray Sciences Division, Argonne National Laboratory, Lemont, Illinois 60439, USA

Note: This paper is part of the JCP Special Topic on The Physical Chemistry of Solar Fuels Catalysis.

a) Author to whom correspondence should be addressed: jlockard@newark.rutgers.edu

ABSTRACT

This study explores the nature, dynamics, and reactivity of the photo-induced charge separated excited state in a Fe³⁺-doped titanium-based metal organic framework (MOF), xFeMIL125-NH₂, as a function of iron concentration. The MOF is synthesized with doping levels x = 0.5, 1and 2 Fe node sites per octameric Ti-oxo cluster and characterized by powder x-ray diffraction, UV-vis diffuse reflectance, atomic absorption, and steady state Fe K-edge X-ray absorption spectroscopy. For each doping level, time-resolved X-ray transient absorption spectroscopy studies confirm the electron trap site role of the Fe sites in the excited state. Time scan data reveal multiexponential decay kinetics for the charge recombination processes which extend into the microsecond range for all three concentrations. A series of dye photodegradation studies, based on the oxidative decomposition of Rhodamine B, demonstrates the reactivity of the charge separated excited state and the photocatalytic capacity of these MOF materials compared to traditional heterometal-doped semiconductor photocatalysts.

Published under an exclusive license by AIP Publishing. https://doi.org/10.1063/5.0174664

I. INTRODUCTION

Materials that exhibit visible light-induced, long-lived charge separation, while possessing a high density of catalytic sites, offer promise as efficient photocatalysts in solar energy applications. This collection of properties is rare however, since small band gap materials with high loading percentages of redox active catalytic sites that participate in the initial rapid charge separation step also tend to yield fast charge recombination rates that compete with more desirable electron transfer processes. Metal-organic frameworks (MOFs), as potential photocatalysts, offer chemical and structural tunability for incorporating high densities of accessible catalytic sites and tailored optoelectronic properties. MOFs are self-assembled, porous, solid state materials composed of metal-based nodes connected in a crystalline network by organic linkers through coordination bonds. 1-5 The presence of transition metal centers with multiple stable oxidation states and linker sites that can accommodate excited state electron transfer are key ingredients for promoting photocatalytic behavior in these materials. Furthermore, linker functionality

and metal node site composition can be altered as a means of tuning the electronic structure and promoting long-lived charge separation behavior for a range of photocatalytic reactions.

MIL-125-NH₂ is a titanium-based MOF, containing octameric metal-oxo clusters connected by aminoterephthalate linkers.^{9,10} Photo-induced linker-to-metal cluster charge transfer (LMCCT) leads to reversible Ti⁴⁺/Ti³⁺ redox conversion at the metal node sites within the framework. Much like the doping strategies used for bandgap engineering in semiconductor materials like TiO₂, 11-1 analogous modifications of Ti-based MOFs can alter their absorption energies and photo redox properties while attempting to avoid high rates of charge recombination. 15-19 The amino linker functionality in MIL-125-NH2 for example, effectively red shifts the LMCCT absorption band into the visible region compared to that of MIL-125, the originally reported, isostructural framework with the non-aminated version linker. This and other reported linker substituents fundamentally tune the overall electronic structure of the MOF by modifying the occupied orbital set, 15,17 leaving the unoccupied orbitals localized on the Ti-oxo nodal cluster primarily intact.

As suggested by theoretical and experimental investigations, 16,18,20 metal cluster composition adjustments should modify these unoccupied frontier orbitals, and therefore the reductive potential of the photoexcited MOF. 15,21 To demonstrate this handle for tuning electronic structure, we recently reported an iron-doped version of MIL-125-NH₂, [MIL-125-NH₂(Ti,Fe)] in which Ti centers within the nodal cluster were substituted with Fe3+ sites using a direct synthesis method.²² This initial investigation, which targeted a doping level of 1 Fe site per cluster, confirmed its coordination at metal-oxo node sites and direct participation in the photoinduced charge separation process. Following LMCCT excitation, the photoexcited electron subsequently localized onto the Fe³⁺ sites, generating long-lived transient Fe²⁺ species. This electron trap site behavior was revealed by Fe K-edge X-ray transient absorption (XTA) spectroscopy, which allows element-specific observation of laserinduced electronic structure changes. XTA has become an important investigative tool for probing the photophysics of molecular²³⁻³³ and solid-state^{34–37} metal-based systems, including other Fe-containing MOFs. 38,39 XTA spectra can reveal transient electronic and geometric structure changes of the absorbing element of interest upon optical laser excitation of the material, while time scan measurements collected at fixed X-ray probe energies provide associated kinetic data.

In this paper, the nature and dynamics of the photo-induced charge separated excited state in xFeMIL125-NH2 are investigated as a function of Fe-doping level, x. Fe K-edge XTA measurements confirm transient electronic reduction of the framework-located Fe sites up to the synthetically accessible doping limit of ~2 Fe sites per cluster. Composite XTA time scan data reveal detailed multiexponential decay kinetics of the charge recombination process extending from the ps to μ s time range. The utility of the proposed electron trap site in photocatalytic applications is demonstrated by a series of dye photodegradation studies. Photodegradation of organic dyes is often used to demonstrate the photocatalytic activity of heterostructure semiconductor⁴⁰⁻⁴⁴ and MOF materials. ^{18,45-48} For the chosen benchmark reaction, photodecomposition of Rhodamine B dye, the Fe-doped MOFs outperformed both MIL125-NH₂(Ti) and Fedoped TiO2 nanoparticles as traditional semiconductor photocatalysts with comparable heterometal content, which has encouraging implications for MOF photocatalysis design strategies.

II. METHODS

A. Materials

Anhydrous methanol and dimethylformamide (DMF) solvents were further dried over molecular sieves prior to use. Anhydrous FeCl₃, Rhodamine B, Acetonitrile, 2-aminoterephthalic acid, Cetyltrimethylammonium Bromide and Titanium (IV) tertbutoxide were used without further purification. Titanium dioxide reference materials were synthesized following literature procedures (see supplementary materials for details).

B. Synthesis

MIL125-NH₂ was synthesized following literature procedures¹⁸ with minor modifications. Briefly, 0.504 g of aminoterephthalic acid dissolved in 12.1 ml of dry DMF and 1.4 ml of dry methanol were added under the flow of nitrogen to a Schlenk flask containing

0.26 ml of Titanium (IV) tert-butoxide. After sonicating for 30 minutes, a spatula tip of Cetyltrimethylammonium Bromide surfactant was added to the mixture, which was then placed in a Teflon lined autoclave and heated to $150\,^{\circ}$ C for 24 h. Once the autoclave had cooled, the MOF suspension was removed and centrifuged at 3000 rpm for 20 min. The solvent supernatant was decanted and replaced with fresh DMF and methanol. This washing procedure was repeated three times before final isolation of the MOF solid. The isostructural MOFs with different target Fe concentrations, xFeMIL125-NH $_2$ were synthesized using a similar procedure except that stoichiometric amounts of anhydrous iron (III) chloride (7.7, 15.4, or 30.8 mg for x = 0.5, 1 and 2 Fe per cluster, respectively) were also dissolved in the DMF solvent prior to addition to the Schenk flask under the flow of nitrogen.

C. Characterization

Powder X-ray diffraction was measured using a Rigaku Miniflex 6G benchtop powder x-ray diffractometer. UV-vis diffuse reflectance spectroscopy (DRS) was measured using a Cary Varian UV-visible–NIR spectrophotometer equipped with a Harrick Scientific Praying Mantis accessory for measuring DRS of powder solid state samples. The iron content in the *x*FeMIL125-NH₂ MOF systems was assessed using a Thermo Scientific iCE 3000 series atomic absorption spectrometer. To prepare samples for AA characterization, MOF samples were activated at 120 °C under vacuum for ~16 h to remove residual DMF solvent prior to digestion in a 20 ml 1:3:6 volumetric ratio solution of 30% hydrogen peroxide, 95% sulfuric acid and water.

D. X-ray transient absorption spectroscopy (XTA)

XTA measurements were carried out at 11-ID-D beamline at the Advanced Photon Source (APS) at Argonne National Lab. The 400 nm laser pump source was obtained from the second harmonic generation of an 800 nm Ti:Sapphire laser with a 10 kHz repetition rate, and 1.6 ps Full Width Half Maximum (FWHM). The x-ray probe pulses were extracted from the APS storage ring under a 24-bunch fill pattern, which consists of 24 singlet pulses with pulse widths of 79 ps and 6.5 MHz repetition rate (i.e. 153.5 ns X-ray pulse spacing). The 400 nm laser pulses were synchronized with respect to the X-ray pulse train. Each liquid suspension sample of the MOF in acetonitrile had ~3.5 mM Fe concentration. Prior to measurement, the suspension samples were first sonicated for 30 min followed by one hour settling time to separate the larger aggregates. The suspension was then decanted into the jet reservoir for circulation and measurement. The final Fe concentration estimated based on the APD signal amplitude was less than 1 mM. The samples were purged with nitrogen and continuously flowed through the 750 μ m diameter jet at a rate of 0.65 ml per second.

The detailed description of the experimental setup and data acquisition procedure has been previously reported. Briefly, fluorescence photons from the sample were collected by two avalanche photodiodes (APDs). A third APD detector collecting elastic scattered X-ray photons was placed near the incoming X-ray beam path and was used as a normalization detector. A multiple X-ray probe data acquisition technique is applied that allows to resolve and record all individual X-ray pulses between two laser excitation pulses. Therefore, a large number of time-resolved XAS spectra can

be acquired simultaneously, with the corresponding time delay t^i (*i* is an integer) of the spectra data set given by the equation:

$$t^i = t^0 + iT_X \tag{1}$$

Where T_x is the X-ray pulse spacing (153.5 ns under APS 24 bunch mode) and t^0 is the time delay of the X-ray pulse closest to the laser, also called the synchronization X-ray pulse. Because of the dilute Fe concentration, a Single Photon Counting (SPC) data acquisition (DAQ) scheme is used.

XAS spectra with the corresponding time delay $t^i > 0$ are designated as "laser on" spectra. XAS spectra from 10 X-ray pulses arriving before the laser excitation were averaged to create the "laser off" spectrum. XTA difference spectra were generated by subtracting "laser off" spectrum from "laser on" spectra at different delays. XAS data were also collected in the absence of laser excitation (i.e. physically blocked laser light) using the sum of all x-ray bunches to generate ground state spectra. Time scans were generated by monitoring the XTA difference signal at fixed energy, 7.121 keV while varying t^0 from -3 to 153.5 ns (i.e. x-ray pulse spacing). The time scan data associated with subsequent x-ray pulses (i > 0) following the synchronized bunch were used to generate longer time kinetics. Beyond the first 24 pulses (i = 0 to 23), the kinetic data from 24 bunches were binned to generate a single averaged time point to increase signal-to-noise at later times. The kinetic traces were fit using a multiexponential decay function convoluted with a gaussian instrument response function with a fixed FWHM equal to the 79 ps x-ray pulse width.

E. Photochemical dye degradation studies

5 mg of MOF were suspended in 20 ml of a 3×10^{-5} M Rhodamine B aqueous solution. The mixture was left to soak for two hours in darkness before photoirradiation by an Optical Building Blocks parabolic reflector xenon arc lamp focused to a spot size of 10 mm diameter. A 400 nm long wave pass colored glass filter and an immersed dielectric IR blocking filter (~700 nm cutoff) were both inserted in the path of the light beam to limit excitation to the visible wavelength region. The power of the filtered lamp light at the sample was recorded as 1.8 W. For wavelength selective RhB degradation experiments, an additional "315-445 nm" bandpass filter was also inserted; or the 400 nm long wave pass filter was replaced with a 550 nm long wave pass filter. The IR blocking filter was used for all irradiation wavelength ranges. The spectra of the resulting filtered irradiation wavelength ranges (400-475 nm and 550-700 nm), measured by an Ocean Optics fiber optic spectrometer, are overlaid with representative DR spectra of the MOF with and without adsorbed RhB dye in Fig. S8. The power was adjusted to be the same for two irradiation wavelength ranges (230 mW measured at the sample focal point). For comparison, the photodegradation reactions were also measured using the full 400-700 nm wavelength range with this lower power (see Fig. S10). For all measurements, suspension samples in glass scintillation vials were placed within the focused light beam and irradiated over the course of 300 min with constant stirring. At regular intervals, 0.5 ml aliquots were retrieved from the vial, and passed through a syringe filter to remove residual suspended photocatalyst prior to measurement. Fixed irradiation time experiments were performed as well and involved 30 min of

continuous irradiation with 400–685 nm light, followed by centrifugation of the suspension sample at 1500 rpm for 5 min. For all experiments, the supernatant aliquot was collected and measured by UV-vis spectroscopy. The efficiency of dye degradation was quantified by measuring the change in absorbance at the peak of the dye absorption band (554 nm).

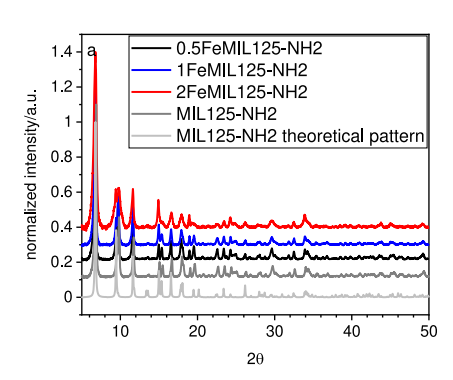
III. RESULTS AND DISCUSSION

A. Characterization

The MIL125-NH2 framework and its Fe-doped versions, 0.5FeMIL125-NH₂, 1FeMIL125-NH₂ and 2FeMIL125-NH₂ were first characterized by powder x-ray diffraction (PXRD), diffuse reflectance (DR), and atomic absorption (AA) spectroscopy. PXRD [Fig. 1(a)] verified the single-phase crystallinity of the Ti-based framework and the Fe-loaded versions up to the maximum doping level of ~2 Fe atoms per cluster. Attempts to introduce higher loading percentages during MOF synthesis were unsuccessful and led to the production of amorphous product. AA analysis of the three Fe-loaded MOFs determined iron weight percentages of 1.87%, 3.42% and 6.64% which translate to 0.57, 1.02 and 1.99 Fe sites per Ti-oxo cluster, respectively, and therefore closely match the target Fe doping levels. The diffuse reflectance spectra of MIL125-NH2 and the Fe-doped versions, shown in Fig. 1(b), all display an absorption band with peak maximum just below 400 nm that extends into the visible wavelength region. This band has been assigned to a n to π^* transition involving the amino linker with additional ligand to metal cluster charge transfer (LMCCT) character. 10,22 Notably, increased absorption of the visible wavelength shoulder relative to the main 400 nm peak is observed upon increased Fe content. While the assignment of this shoulder is not definitive, its enhancement may arise from LMCT transitions with direct involvement of the Fe sites, ligand field Fe d-d transitions, or a combination of both. Steady state XAS spectra collected in the absence of laser excitation are shown in Fig. S3. All three Fe-doped MOFs display nearly identical spectra, consistent with that we previously reported for 1FeMIL125-NH₂,²² indicating analogous 3+ oxidation state and local coordination geometry of the Fe dopants, confirming their substitution for Ti in octahedrally coordinated metal oxo cluster sites of the MOF, in each case.

B. XTA results

The XTA spectra for the 1FeMIL125-NH₂ system collected at pre-time zero ("laser off") and at 100 ps time delay (i.e., nominal time zero, denoted "laser on") are shown in Fig. 2 along with the XTA difference spectra obtained at this and later time delays. A significant shift in the rising edge towards a lower energy is observed between the laser on and laser off spectra. The change is exemplified by the XTA difference spectra measured at positive time delays, which exhibit the characteristic derivative like shape associated with an edge shift to lower energy. These spectral changes are consistent with our previously reported results for this framework obtained using the hybrid fill pattern for the X-ray probe²² and denote the presence of transiently reduced iron sites upon photoexcitation. The persistence of the difference signal into the microsecond time range provides evidence that photoinduced



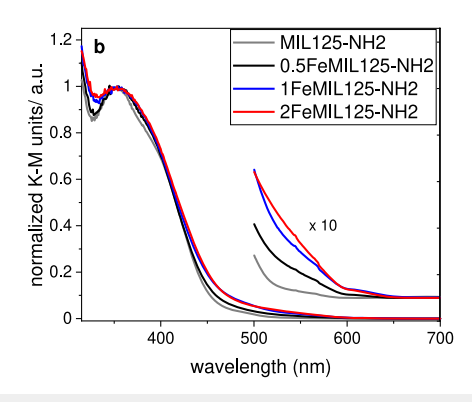


FIG. 1. (a) PXRD patterns and (b) Normalized DR spectra of MIL125-NH₂, 0.5FeMIL125-NH₂, 1FeMIL125-NH₂, 2FeMIL125-NH₂.

LMCCT leads to long-lived charge separation through the localization of the electron onto these metal sites within the MOF clusters. All three iron doping concentrations exhibit similar XTA spectral trends (0.5FeMIL125-NH₂ and 2FeMIL125-NH₂ are shown in Fig. S4 in the supplementary material), signifying that the long-lived charge separation is preserved even at higher doping levels.

Using the standard operating mode for the X-ray probe (i.e., 24-bunch fill pattern that contains X-ray bunches spaced at 153 ns intervals) allowed us to map more accurately and efficiently the decay over several decades of time delays. Time scans collected by monitoring the XTA difference signal at 7.121 keV for each Fe concentration sample are shown in Fig. 2 (and Fig. S5 in the supplementary material). The kinetic data associated with all 24 bunches over the course of six orbits following the synchronized bunch/orbit were combined to give the total kinetic trace to 22 μ s.

Table I summarizes the results of the kinetic fits achieved using a multiexponential decay model with an amplitude shelf, A_{∞} at long delay times. Following fast photoinduced charge separation that localizes electrons on the Fe sites, the decay in each case arises from the recombination of these electrons with the linker-located holes. The multiple lifetime components of this decay, which span the ps to microsecond time range, are not surprising given the range of potential charge recombination pathways in these

frameworks. The long delay time shelf for each system indicates the preservation of the charge-separated excited state beyond the measurable delay time range, far into the microsecond time regime. While similar decay trends are observed across all three iron doping levels, the weighted average decay lifetime obtained for 2FeMIL125-NH₂ is slightly shorter and its amplitude shelf at long delay time is significantly lower than those observed for the 0.5Fe or 1FeMIL125-NH2 frameworks. These observations are consistent with the higher rate of charge recombination expected with an increased number of iron sites and therefore higher probability of electron-hole recombination. Compared to doped semiconductor materials like TiO₂, these MOF clusters appear able to accommodate a far higher heterometal dopant concentration before charge recombination processes start to curtail the lifetime of the charge-separated excited state. In contrast, doped semiconductors like Fe-doped TiO₂, reportedly undergoes rapid charge recombination at dopant concentrations above only 1%. 50,51 While the mechanism in this material is likely quite different, with the Fe sites potentially serving as both electron, Fe²⁺ and hole, Fe⁴⁺ traps, the trend remains: when comparably high Fe doping levels are involved, the charge separated excited state lifetime in Fe-doped TiO2 is drastically reduced compared to that in the Fe-doped MOFs reported here. The XTA measurements show that long lived charge separation is preserved for

TABLE I. Fitting parameters for the xFeMIL125-NH₂ XTA kinetics.

	0.5FeMIL125-NH ₂	1FeMIL125-NH ₂	2FeMIL125-NH ₂
$\overline{A_1}$	0.290 ± 0.036 5	0.367 ± 0.367	0.242 ± 0.017 5
τ_1	$0.000~97 \pm 0.000~21~\mu s$	$0.000\ 97 \pm 0.000\ 1\ \mu s$	$0.000\ 52\pm0.000\ 08\ \mu s$
A_2	0.258 ± 0.039	0.169 ± 0.0209	$0.291 \pm 0.019 6$
τ_2	$0.010\ 6\pm0.002\ 74\ \mu s$	$0.019~0 \pm 0.006~45~\mu s$	$0.006\ 38 \pm 0.000\ 79\ \mu s$
A_3	0.116 ± 0.0149	$0.146 \pm 0.016 \ 1$	$0.173 \pm 0.010 \ 7$
τ_3	$0.396 \pm 0.106 \mu s$	$0.463 \pm 0.109 \mu s$	$0.233 \pm 0.028 4 \mu s$
A_4	0.193 ± 0.00895	0.180 ± 0.00824	$0.197 \pm 0.005 \stackrel{\cdot}{65}$
τ_4	$8.13 \pm 1.312 \mu s$	$8.77 \pm 1.519 \mu s$	$7.84 \pm 0.755 \mu s$
τ_{avg}^{a}	$1.89 \pm 0.311 \mu s$	$1.91 \pm 0.336 \mu s$	$1.76 \pm 0.170 \mu s$
A_{∞}	0.104 ± 0.00927	0.0927 ± 0.00969	0.0549 ± 0.00575

^aWeighted average of the four lifetime components.

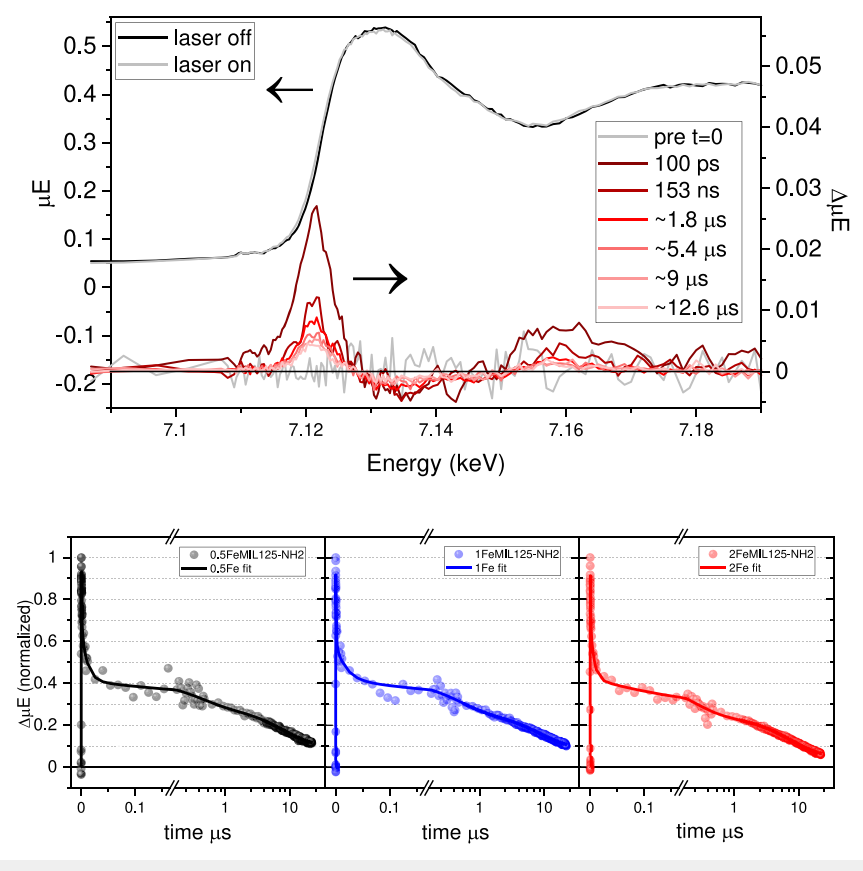


FIG. 2. Top: laser off (black) and laser on (grey) XTA spectra of 1FeMIL125-NH₂ along with corresponding XTA difference spectra obtained at nominal time zero and subsequent time delays. Bottom: XTA kinetic data collected at 7.121 keV with multiexponential fits for 0.5, 1, and 2FeMIL125-NH₂. Kinetic data are normalized to their respective maxima.

Fe-doped MIL125-NH₂, even at Fe concentration levels as high as nearly 7%.

C. Photodegradation of Rhodamine B dye

The photochemical degradation of Rhodamine B in the presence of Fe-doped MIL125-NH2 demonstrates the correlation between the charge separated excited states with increased number of electron (and hole) trap sites and their ultimate reactivity. This reaction serves as a convenient benchmark as it has been used to test the photoreactivity of other MIL125-NH₂-based MOF materials.⁴ Here, the depletion of Rhodamine B in the presence of different photocatalysts under visible light irradiation is monitored by UV-vis spectroscopy. As shown in Fig. 3 and Table II, the Fe-containing MOFs led to a marked decrease in dye concentration, with increased degradation efficiency tracking with increased Fe content, while the Fe-TiO₂ nanoparticle reference photocatalysts elicited far slower rates of dye depletion. Undoped MIL125-NH2 also exhibits dye degradation behavior, nearly on par with that of 0.5FeMIL125-NH₂ but is significantly less effective than the 1Fe and 2Fe per cluster doped MOFs. This demonstrates that the addition of iron sites into the framework has a substantial effect on the electronic structure, and as previously hypothesized, the presence of accessible Fe trap sites allows for much more efficient redox reactions. In fact, some reactivity enhancement is observed with increasing Fe content in this framework even in the absence of light (as illustrated in Fig. 3 by the "dark" measurements collected prior to the start of irradiation time t=0), suggesting that the readily accessible Fe³⁺ sites may serve as direct oxidants in degrading the dye.

The Fe-TiO₂ nanoparticle photocatalyst demonstrated better reactivity than the parent TiO₂ nanoparticle reference but with a far slower rate of dye degradation than that of the MOF series, even while possessing a similar Fe concentration as the most active MOF, 2FeMIL125-NH₂. The "optimum" Fe doping level in TiO₂ semiconductor material for efficient photocatalysis is typically reported to be around 1%, ⁵² The Fe-TiO₂ reference measured in this work contained an iron weight percentage of about 5 wt. %. At this doping level in TiO₂, photocatalytic efficiencies would be expected to drop since charge recombination mechanisms start to compete with the charge migration and interfacial electron transfer processes of the photoreaction. By comparison, 2FeMIL125-NH₂ contains 6.7 wt. % Fe and displayed the highest photodegradation efficiency. With dye molecules capable of diffusing into the porous structure, we contend that electron-hole pairs can be used essentially at the point

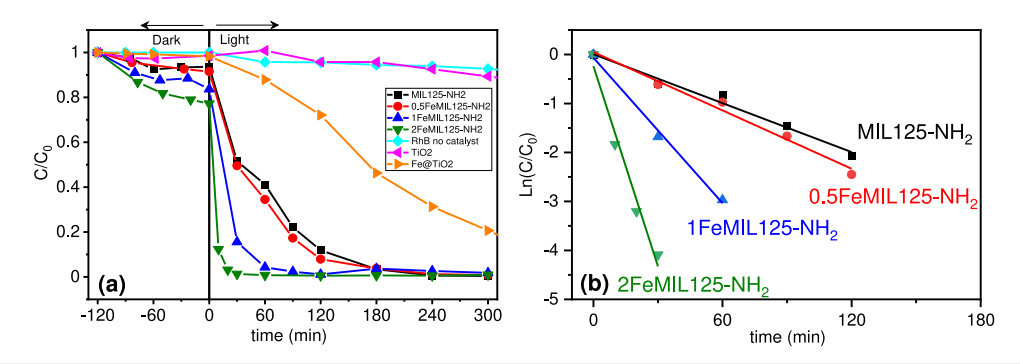


FIG. 3. Upon photoirradation with 400–700 nm light, (a) normalized concentration of Rhodamine B over time as monitored by UV-vis spectroscopy where C_0 is the concentration of RhB at t = -120 min (b) plot of $\ln(C/C_0)$ vs time with linear fit showing pseudo-first order kinetics for photodegradation of RhB, $[\ln(C/C_0) = -kt]$ where C_0 is the concentration of RhB at t = 0 min.

TABLE II. Fe concentrations, dye degradation efficiencies for MIL125-NH2 and reference photocatalysts.

Photocatalyst	%wt Fe ^a (%)	Average dye degradation efficiency ^b (%)	Degradation reaction rate constant ^c (min ⁻¹)
MIL125-NH ₂	0	18.2 ± 1.3	0.0167
0.5FeMIL125-NH ₂	1.7	22.8 ± 0.9	0.0199
1FeMIL125-NH ₂	3.4	70.9 ± 0.48	0.0495
2FeMIL125-NH ₂	6.7	93.9 ± 0.81	0.136
TiO_2	0	2.31 ± 1.82	•••
Fe-TiO ₂	5.0	4.80 ± 1.28	

^aDetermined by atomic absorption spectroscopy.

of photogeneration, rendering charge migration unnecessary (or at least non-rate limiting). The XTA results shown above also confirm extended charge separated excited state lifetimes even at much higher iron doping concentrations, indicating that MIL125-NH₂ can accommodate far higher Fe loading percentages before charge recombination rates become prohibitively rapid. Notably, the XTA decay kinetics are similar across all three Fe concentrations and only begin to deviate at longer times (microsecond time regime). On a timescale more in line with that of typical diffuse intermolecular charge transfer processes, like those involved in the dye degradation reactions (on the order of ~10–100 ns), the XTA difference signals are nearly equivalent across all three Fe concentrations. This suggests that the transiently reduced Fe²⁺ site concentration, and therefore the reactivity, scales with the total Fe doping level.

The other important factors likely contributing to the enhanced visible light photocatalytic behavior of the MOF materials compared to the TiO₂ reference systems are the differences in absorption cross section in this spectral wavelength range and sensitization behavior of the adsorbed dye. While Fe (and other transition metal) doping serves to lower the bandgap of the TiO₂ semiconductor (see Fig. S1 in the supplementary material), the effect is less significant than that of the amino-functionalized linkers in the MIL125-NH₂ series,

which extend the LMCCT band into the visible region. Doping the clusters of this framework with Fe further redshifts the absorption band producing an even lower effective bandgap compared to the Fe-TiO $_2$ system.

The established mechanism for photocatalytic dye degradation follows an indirect process in which both electrons and holes of the photoinduced charge separated state of the photocatalyst can act to generate OH· radicals in the presence of water and oxygen.⁵³ These hydroxyl radicals, in turn, break apart the dye molecules through a series of oxidation steps. If dye molecules adsorbed on the surface (or within the pores) of the photocatalyst are also excited, as is likely the case when visible light irradiation wavelengths are used, then they too can participate in the dye degradation process via self-sensitization. 54-56 Photoexcited, adsorbed dye molecules can undergo interfacial electron transfer to the catalyst, producing unstable dye cation radicals susceptible to attack by reactive superoxide radical, O2 - species concurrently generated by the charge injected photocatalyst. While previous dye degradation studies of MIL125-NH2-based photocatalysts have not implicated this self-sensitization component of the RhB degradation process, 45,48 its contribution cannot be ignored, particularly if the dye molecules are strongly adsorbed to the photocatalyst.⁵⁷ Fig. S7 in the supplementary material shows the DR spectra of the isolated

^bMesaured in triplicate, evaluated after 30 min irradiation time.

^cAsuming pseudo-first order kinetics, $[\ln(C/C_0) = -kt]$.

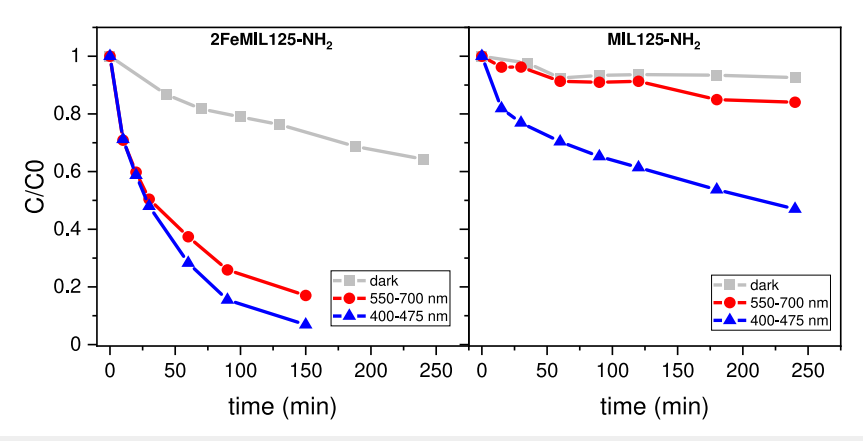


FIG. 4. Wavelength dependent Rhodamine B dye photodegradation observed over time obtained using undoped MIL125-NH₂ (right) and 2FeMIL125-NH₂ (left) photocatalyst. Dye degradation observed in the presence of each catalyst yet absence of light is overlaid for comparison in each case.

RhB-loaded photocatalysts after extensive washing. The spectra of MIL125-NH₂ and all three Fe-doped frameworks display the RhB absorption band, which is redshift compared to the spectrum of the dye in solution. The persistence of the band even after washing indicates strong RhB dye adsorption within these frameworks. Its bathochromic shift suggests J-aggregate formation,⁵⁷ an alignment likely imposed by the pores of the structure. For the TiO₂ materials, however, following the same dye loading and washing procedure, the RhB absorption band is nearly absent, indicating significantly weaker dye adsorption to the semiconductor nanoparticles compared to the MIL125-NH₂ materials.

To help establish the relative contribution of RhB selfsensitization to its photodegradation process for the MOF photocatalysts, we compared the dye depletion rate measured using different irradiation wavelength ranges to selectively excite either the LMCCT state of the framework or the π - π * state of the adsorbed RhB dye. As illustrated in Fig. 4, direct irradiation of the LMCCT band of MIL125-NH2 (400-475 nm) led to more efficient dye degradation compared to that associated with the selective dye excitation (550-700 nm), which showed minimal evidence of selfsensitized photodegradation. For the Fe-doped MIL125-NH2 photocatalysts however, the two excitation wavelength ranges led to similar dye degradation responses (Figs. 4 and S9 in the supplementary material). While not entirely definitive, since there is some spectral overlap of the MOF and dye adsorption bands, the fact that preferential photoirradiation of either the LMCCT state of the MOF or the π - π * transition of the dye itself produced similar results suggests that both excitation routes play a role in the dye degradation process for the Fe-doped MOFs.

IV. CONCLUSIONS

The results of this study demonstrate that the porous nature of the framework, along with the metal node location of the iron trap sites permits a higher doping level of accessible catalytic sites that avoid fast charge recombination and the need for long-range charge transport. XTA measurements confirmed the transient reduction of the Fe sites and its long-lived nature across a range of concentrations while the dye photodegradation studies revealed their relative reactivity, and likely enhancment of the dye self-sensitization

contribution to the degradation process. In this framework, the upper limit of Fe doping level was dictated by the synthesis, rather than a decline in charge recombination lifetime or photocatalytic performance. Attempted Fe loading percentages above 6.7% started to interfere with MOF structure formation, leading to an amorphous product. However, this MOF system provides a blueprint for designing frameworks to accommodate heterometals with higher concentrations for efficient photocatalysis applications. Furthermore, the enhanced uptake of the RhB dye in the MOF under mild incubation conditions presents an opportunity to further enhance visble light absorption via dye sensitization, provided more robust dyes are employed.

SUPPLEMENTARY MATERIAL

See supplementary material for synthesis procedures and characterization results for ${\rm TiO_2}$ nanoparticle reference materials, PXRD data, steady state XAS and additional XTA results, additional DR and dye photodegradation results.

ACKNOWLEDGMENTS

This material is based upon work supported by the National Science Foundation under Grant No. DMR-2003910. Supplement funding for this project was provided by the Rutgers University – Newark Chancellor's Research Office. This research used resources of the Advanced Photon Source, an Office of Science User Facility operated for the U.S. Department of Energy (DOE) Office of Science by Argonne National Laboratory, and was supported by the U.S. DOE under Contract No. DE-AC02-06CH11357.

AUTHOR DECLARATIONS

Conflict of Interest

The authors have no conflicts to disclose.

Author Contributions

Conor L. Long: Conceptualization (lead); Data curation (equal); Formal analysis (supporting); Writing – original draft (supporting);

Writing – review & editing (supporting). Xiaoyi Zhang: Formal analysis (supporting); Investigation (supporting); Methodology (supporting); Resources (supporting); Writing – review & editing (supporting). Jenny V. Lockard: Conceptualization (lead); Data curation (supporting); Formal analysis (lead); Funding acquisition (lead); Writing – original draft (lead); Writing – review & editing (lead).

DATA AVAILABILITY

The data that support the findings of this study are available within the article and its supplementary material.

REFERENCES

- ¹H. Furukawa, K. E. Cordova, M. O'Keeffe, and O. M. Yaghi, Science **341**(6149), 1230444 (2013).
- ²G. K. Kole and J. J. Vittal, Chem. Soc. Rev. **42**(4), 1755–1775 (2013).
- ³ M. L. Foo, R. Matsuda, and S. Kitagawa, Chem. Mater. **26**(1), 310–322 (2014).
- ⁴C. Wang, D. Liu, and W. Lin, J. Am. Chem. Soc. 135(36), 13222–13234 (2013).
- ⁵S. Yuan, L. Feng, K. Wang, J. Pang, M. Bosch, C. Lollar, Y. Sun, J. Qin, X. Yang, P. Zhang, Q. Wang, L. Zou, Y. Zhang, L. Zhang, Y. Fang, J. Li, and H.-C. Zhou, Adv. Mater. 30(37), 1704303 (2018).
- ⁶L. Zeng, X. Guo, C. He, and C. Duan, ACS Catal. **6**(11), 7935–7947 (2016).
- ⁷L. Shen, S. Liang, W. Wu, R. Liang, and L. Wu, Dalton Trans. 42(37), 13649–13657 (2013).
- ⁸D. Sun, L. Ye, and Z. Li, Appl. Catal., B 164, 428–432 (2015).
- ⁹M. Dan-Hardi, C. Serre, T. Frot, L. Rozes, G. Maurin, C. Sanchez, and G. Férey, J. Am. Chem. Soc. **131**(31), 10857–10859 (2009).
- ¹⁰ Y. Fu, D. Sun, Y. Chen, R. Huang, Z. Ding, X. Fu, and Z. Li, Angew. Chem., Int. Ed. 51(14), 3364–3367 (2012).
- ¹¹Y. Cong, J. Zhang, F. Chen, and M. Anpo, J. Phys. Chem. C **111**(19), 6976–6982 (2007)
- ¹² A. Di Paola, E. Garcia-López, S. Ikeda, G. Marcí, B. Ohtani, and L. Palmisano, Catal. Today 75(1–4), 87–93 (2002).
- ¹³S. N. R. Inturi, T. Boningari, M. Suidan, and P. G. Smirniotis, Appl. Catal., B 144, 333–342 (2014).
- ¹⁴Y. Matsumoto, M. Murakami, T. Shono, T. Hasegawa, T. Fukumura, M. Kawasaki, P. Ahmet, T. Chikyow, S.-y. Koshihara, and H. Koinuma, Science 291(5505), 854–856 (2001).
- ¹⁵C. H. Hendon, D. Tiana, M. Fontecave, C. Sanchez, L. D'arras, C. Sassoye, L. Rozes, C. Mellot-Draznieks, and A. Walsh, J. Am. Chem. Soc. 135(30), 10942–10945 (2013).
- ¹⁶Y. Fu, H. Yang, R. Du, G. Tu, C. Xu, F. Zhang, M. Fan, and W. Zhu, RSC Adv. 7(68), 42819–42825 (2017).
- ¹⁷ M. W. Logan, S. Ayad, J. D. Adamson, T. Dilbeck, K. Hanson, and F. J. Uribe-Romo, J. Mater. Chem. A 5(23), 11854–11863 (2017).
- ¹⁸D. Ao, J. Zhang, and H. Liu, J. Photochem. Photobiol., A 364, 524–533 (2018).
- ¹⁹R. M. Abdelhameed, M. M. Q. Simões, A. M. S. Silva, and J. Rocha, Chem. -Eur. J. 21(31), 11072–11081 (2015).
- ²⁰ M. A. Syzgantseva, C. P. Ireland, F. M. Ebrahim, B. Smit, and O. A. Syzgantseva, J. Am. Chem. Soc. **141**(15), 6271–6278 (2019).
- ²¹ M. A. Nasalevich, C. H. Hendon, J. G. Santaclara, K. Svane, B. van der Linden, S. L. Veber, M. V. Fedin, A. J. Houtepen, M. A. van der Veen, F. Kapteijn, A. Walsh, and J. Gascon, Sci. Rep. **6**(1), 23676 (2016).
- ²²L. Hanna, C. L. Long, X. Zhang, and J. V. Lockard, Chem. Commun. 56(78), 11597–11600 (2020).
- ²³C. Bressler, C. Milne, V. T. Pham, A. ElNahhas, R. M. van der Veen, W. Gawelda, S. Johnson, P. Beaud, D. Grolimund, M. Kaiser, C. N. Borca, G. Ingold, R. Abela, and M. Chergui, Science 323(5913), 489 (2009).
- ²⁴ A. Cannizzo, C. J. Milne, C. Consani, W. Gawelda, C. Bressler, F. van Mourik, and M. Chergui, Coord. Chem. Rev. 254(21-22), 2677–2686 (2010).

- ²⁵ L. X. Chen, W. J. H. Jäger, G. Jennings, D. J. Gosztola, A. Munkholm, and J. P. Hessler, Science 292(5515), 262–264 (2001).
- ²⁶ L. X. Chen, G. B. Shaw, I. Novozhilova, T. Liu, G. Jennings, K. Attenkofer, G. J. Meyer, and P. Coppens, J. Am. Chem. Soc. 125(23), 7022–7034 (2003).
- ²⁷H. Cho, M. L. Strader, K. Hong, L. Jamula, E. M. Gullikson, T. K. Kim, F. M. F. de Groot, J. K. McCusker, R. W. Schoenlein, and N. Huse, Faraday Discuss. 157(0), 463–474 (2012).
- ²⁸ W. Gawelda, V.-T. Pham, M. Benfatto, Y. Zaushitsyn, M. Kaiser, D. Grolimund, S. L. Johnson, R. Abela, A. Hauser, C. Bressler, and M. Chergui, Phys. Rev. Lett. 98(5), 057401 (2007).
- ²⁹ J. V. Lockard, A. A. Rachford, G. Smolentsev, A. B. Stickrath, X. Wang, X. Zhang, K. Atenkoffer, G. Jennings, A. Soldatov, A. L. Rheingold, F. N. Castellano, and L. X. Chen, J. Phys. Chem. A 114(48), 12780–12787 (2010).
- ³⁰ M. L. Shelby, M. W. Mara, and L. X. Chen, Coord. Chem. Rev. 277-278, 291-299 (2014).
- 31G. Smolentsev and V. Sundström, Coord. Chem. Rev. 304-305, 117-132 (2015).
- ³² R. van der Veen, C. J. Milne, A. El Nahhas, F. A. Lima, V.-T. Pham, J. Best, J. A. Weinstein, C. N. Borca, R. Abela, C. Bressler, and M. Chergui, Angew. Chem., Int. Ed. 48(15), 2711–2714 (2009).
- 33 L. X. Chen, Angew. Chem., Int. Ed. 43(22), 2886–2905 (2004).
- ³⁴J. Huang, O. Buyukcakir, M. W. Mara, A. Coskun, N. M. Dimitrijevic, G. Barin, O. Kokhan, A. B. Stickrath, R. Ruppert, D. M. Tiede, J. F. Stoddart, J.-P. Sauvage, and L. X. Chen, Angew. Chem., Int. Ed. 51(51), 12711–12715 (2012).
- ³⁵B. Pattengale, S. Yang, J. Ludwig, Z. Huang, X. Zhang, and J. Huang, J. Am. Chem. Soc. 138(26), 8072–8075 (2016).
- ³⁶F. Zamponi, T. J. Penfold, M. Nachtegaal, A. Lubcke, J. Rittmann, C. J. Milne, M. Chergui, and J. A. van Bokhoven, Phys. Chem. Chem. Phys. **16**(42), 23157–23163 (2014)
- ³⁷X. Zhang, G. Smolentsev, J. Guo, K. Attenkofer, C. Kurtz, G. Jennings, J. V. Lockard, A. B. Stickrath, and L. X. Chen, J. Phys. Chem. Lett. 2(6), 628–632 (2011).
 ³⁸L. Hanna, P. Kucheryavy, C. Liu, X. Zhang, and J. V. Lockard, J. Phys. Chem. C 121(25), 13570–13576 (2017).
- ³⁹ J. Nyakuchena, S. Ostresh, J. Neu, D. Streater, C. Cody, R. Hooper, X. Zhang, B. Reinhart, G. W. Brudvig, and J. Huang, J. Phys. Chem. Lett. **14**(26), 5960–5965 (2023).
- ⁴⁰Y.-H. Chiu, T.-F. M. Chang, C.-Y. Chen, M. Sone, and Y.-J. Hsu, Catalysts 9(5), 430 (2019).
- ⁴¹Y. Y. Lee, J. H. Moon, Y. S. Choi, G. O. Park, M. Jin, L. Y. Jin, D. Li, J. Y. Lee, S. U. Son, and J. M. Kim, J. Phys. Chem. C **121**(9), 5137–5144 (2017).
- ⁴²S. Harish, J. Archana, M. Navaneethan, S. Ponnusamy, A. Singh, V. Gupta, D. K. Aswal, H. Ikeda, and Y. Hayakawa, RSC Adv. 7(55), 34366–34375 (2017)
- ⁴³T. T. Le, M. S. Akhtar, D. M. Park, J. C. Lee, and O. B. Yang, Appl. Catal., B **111-112**, 397-401 (2012).
- ⁴⁴L. Pan, J.-J. Zou, S. Wang, Z.-F. Huang, X. Zhang, and L. Wang, Appl. Surf. Sci. 268, 252–258 (2013).
- ⁴⁵H.-T. Nguyen Thi, K.-N. Tran Thi, N. B. Hoang, B. T. Tran, T. S. Do, C. S. Phung, and K.-O. Nguyen Thi, Materials **14**(24), 7741 (2021).
- ⁴⁶Z. Wu, X. Yuan, J. Zhang, H. Wang, L. Jiang, and G. Zeng, ChemCatChem **9**(1), 41–64 (2017).
- ⁴⁷L. Ai, C. Zhang, L. Li, and J. Jiang, Appl. Catal., B **148-149**, 191–200 (2014).
- ⁴⁸S. Hu, M. Liu, K. Li, C. Song, G. Zhang, and X. Guo, RSC Adv. 7(1), 581–587 (2017).
- ⁴⁹E. D. Kinigstein, G. Jennings, C. A. Kurtz, A. M. March, X. Zuo, L. X. Chen, K. Attenkofer, and X. Zhang, Rev. Sci. Instrum. 92(8), 085109 (2021).
- ⁵⁰ H. Moradi, A. Eshaghi, S. R. Hosseini, and K. Ghani, Ultrason. Sonochem. 32, 314–319 (2016).
- ⁵¹ W. Choi, A. Termin, and M. R. Hoffmann, J. Phys. Chem. **98**(51), 13669–13679 (1994).
- ⁵²T. Tong, J. Zhang, B. Tian, F. Chen, and D. He, J. Hazard. Mater. 155(3), 572–579 (2008).
- ⁵³ A. Ajmal, I. Majeed, R. N. Malik, H. Idriss, and M. A. Nadeem, RSC Adv. 4(70), 37003–37026 (2014).

 ⁵⁴Z. Wu, X. Yuan, G. Zeng, L. Jiang, H. Zhong, Y. Xie, H. Wang, X. Chen, and H. Wang, Appl. Catal., B 225, 8–21 (2018).
 ⁵⁵T. Watanabe, T. Takizawa, and K. Honda, J. Phys. Chem. 81(19), 1845–1851

 $^{^{\}bf 56}$ M. Nussbaum, N. Shaham-Waldmann, and Y. Paz, J. Photochem. Photobiol., A

⁵⁷J. P. Cassidy, J. A. Tan, and K. L. Wustholz, J. Phys. Chem. C **121**(29), 15610–15618 (2017).